Nanoscale Advances

COMMUNICATION

View Article Online
View Journal | View Issue

Cite this: *Nanoscale Adv.*, 2019, **1**, 953

Received 17th September 2018
Accepted 5th November 2018

DOI: 10.1039/c8na00212f

rsc.li/nanoscale-advances

Effects of precursor pre-treatment on the vapor deposition of WS_2 monolayers†

Mei Er Pam,[ab] Yumeng Shi,*[acd] Junping Hu,[a] Xiaoxu Zhao,[e] Jiadong Dan,[e] Xue Gong,[ac] Shaozhuan Huang,[a] Dechao Geng,[a] Stephen Pennycook,[fg] Lay Kee Ang[ab] and Hui Ying Yang*[a]

Transition metal oxide powders have been widely used as the growth precursors for monolayer transition metal dichalcogenides (TMDCs) in chemical vapor deposition (CVD). It has been proposed that metal oxide precursors in the gas phase undergo a two-step reaction during CVD growth, where transition metal sub-oxides are likely formed first and then the sulfurization of these sub-oxides leads to the formation of TMDCs. However, the effects of stoichiometry of transition metal oxide precursors on the growth of TMDC monolayers have not been studied yet. In this contribution, we report the critical role of the WO_3 precursor pre-annealing process on the growth of WS_2 monolayers. Besides, several WO_3 precursors with different types of oxygen vacancies have also been prepared and investigated by X-ray powder diffraction (XRD), X-ray photoelectron spectroscopy (XPS) and density functional theory calculation. Among all the non-stoichiometric WO_3 precursors, thermally annealed WO_3 powder exhibits the highest oxygen vacancy concentration and produces WS_2 monolayers with significantly improved quality in terms of lateral size, density, and crystallinity. Our comprehensive study suggests that the chemical composition of transition metal oxide precursors would be fundamentally critical for the growth of large-area and high-quality WS_2 monolayers, which further pave the way for revealing their intrinsic properties and unique applications.

Introduction

The extraordinary electrical, optical, thermal and mechanical properties, which exist in monolayer transition metal dichalcogenides (TMDC) materials, offer various promising applications in future ultrathin logic devices, nanogenerators, flexible electronics and optoelectronic devices.[1–4] Specifically, the tunable properties of band offset, carrier density,[5] and band gap[6–8] make TMDCs one of the most extensively researched subjects for practical and fundamental studies. Monolayer tungsten disulfide (WS_2) has been intensively studied as a next generation nanoelectronic and optoelectronic material due to its indirect to direct band gap tunability,[9,10] high on/off current ratio,[11,12] high thermal stability,[13] excellent electrostatic integrity[14] and strong photoluminescence.[15,16] Additionally, WS_2 monolayers have shown an interesting spin orbit coupling effect resulting from the breaking of inversion symmetry of their crystal lattices, and the strong magnetic field interaction in WS_2 monolayers favors their applications in optoelectronic and spintronic devices.[17,18]

Various approaches have been employed to prepare WS_2 monolayers. The layered structure of WS_2 allows the mechanical or chemical exfoliation of monolayer crystals from their bulk counterparts. However, the exfoliated flakes show random thickness, size and shape that create great difficulties in large scale industrial applications.[16] Chemical vapor deposition (CVD) has been widely adapted as one of the most effective strategies to grow wafer-scale two-dimensional (2D) materials including graphene, boron nitride, and TMDCs.[19–23] In the pioneering studies of monolayer WS_2 synthesis, tungsten trioxide (WO_3) powder was chosen as the growth precursor and a low concentration of hydrogen (H_2) gas was usually introduced to reduce WO_3 to tungsten suboxide.[22,24,25] Nevertheless, excessive hydrogen supply could also have an etching effect and

[a]*Pillar of Engineering Product Development, Singapore University of Technology and Design, 8 Somapah Road, Singapore 487372, Singapore. E-mail: yanghuiying@sutd.edu.sg*

[b]*Science and Math Cluster, Singapore University of Technology and Design, 8 Somapah Road, Singapore 487372, Singapore*

[c]*International Collaborative Laboratory of 2D Materials for Optoelectronic Science & Technology of Ministry of Education, Engineering Technology Research Center for 2D Material Information Function Devices and Systems of Guangdong Province, College of Optoelectronic Engineering, Shenzhen University, Shenzhen 518060, China*

[d]*Engineering Technology Research Center for 2D Material Information Function Devices and Systems of Guangdong Province, College of Optoelectronic Engineering, Shenzhen University, Shenzhen 518060, China*

[e]*Department of Chemistry, National University of Singapore, 3 Science Drive 3, Singapore 117543, Singapore*

[f]*Department of Materials Science and Engineering, National University of Singapore, 9 Engineering Drive 1, Singapore 117575, Singapore*

[g]*NUS Graduate School for Integrative Sciences and Engineering, National University of Singapore, 13 Centre for Life Science, #05-01, 28 Medical Drive, Singapore 117456, Singapore*

† Electronic supplementary information (ESI) available. See DOI: 10.1039/c8na00212f

induce various structural defects in monolayer WS_2.[16,25,26] Traditionally, tungsten oxides have been intensively studied previously for photocatalysis,[27,28] electrochemistry,[29] electrochromic application,[30,31] *etc*. According to the literature, WO_3 powder is usually found in a non-stoichiometric composition and the W element may show various chemical states due to the spontaneous reduction of WO_3 under ambient conditions.[30] It has been demonstrated that the sulfurization process of transition-metal suboxides in the CVD process plays a critical role in the nucleation and crystallization of TMDC monolayers.[22,32]

In the CVD process, the generation and evolution of transition metal sub-oxide species can significantly affect the morphology and edge structure of TMDCs, which lead to dramatically different optical, electronical and magnetic properties.[20] However, the study of the effects of chemical composition of WO_3 on the CVD growth of WS_2, in terms of quality, morphology and optical properties, is still lacking. Herein, we prepared various tungsten oxide precursors with different oxygen vacancy concentrations, that is, commercially available fresh WO_3 (FWO_3), thermally annealed WO_3 (AWO_3), air plasma treated WO_3 ($PTWO_3$) and thermally annealed $PTWO_3$ powder ($PTAWO_3$) to provide tungsten suboxide sources. The results reveal that AWO_3 powder with the highest oxygen vacancy content produces WS_2 monolayers with significantly improved domain size, higher coverage density, and higher crystallinity. Besides, we further demonstrate that the use of AWO_3 powder instead of the introduction of hydrogen gas during the growth of monolayer WS_2 to provide a tungsten suboxide source will enhance the growth of monolayer WS_2 and produce monolayer WS_2 with suppressed atomic defects. The control synthesis of WS_2 monolayers by precursor pretreatment provides further insights into the growth mechanism and enables the production of WS_2 monolayers with high quality for the development of a broad range of optoelectronic and electronic applications.

Experimental methods

Preparation of tungsten trioxide (WO_3) precursors

The WO_3 precursors were pretreated with heat, air plasma or both. Four WO_3 precursors prepared with different methods were studied for comparison, including commercially available WO_3 (FWO_3) (Sigma-Aldrich), thermally annealed WO_3 (AWO_3), air plasma treated WO_3 ($PTWO_3$) and plasma treated annealed WO_3 ($PTAWO_3$) powder.

For AWO_3 powder, 500 mg of WO_3 powder was loaded in an alumina boat, placed at the center of a furnace, and heated up to 500 °C in air for 30 minutes.

For $PTWO_3$ powder, 500 mg of WO_3 powder was loaded in an alumina boat, placed at the center of a plasma reactor center (Plasma Cleaner PDC-32G-2). The sample was directly exposed to a direct inductively coupled plasma. During the plasma treatment process, the chamber was evacuated to 1.5 mTorr with a mechanical pump and the radio frequency power was turned to ~18 W, and at the same time air was introduced into the chamber and the process was continued for 5 minutes.

For $PTAWO_3$ powder, 500 mg of WO_3 powder was first treated using air plasma with the same preparation steps as the plasma treated WO_3 powder, and the powder was then annealed using the same procedure that we employed to prepare the annealed WO_3 powder sample.

Growth process of monolayer WS_2

The employed CVD process for monolayer WS_2 is based on our previous report.[33,34] Prior to the growth process, single-side polished sapphire substrates were washed with the solution mixture of H_2SO_4 and H_2O_2 and blow-dried with nitrogen gas. An alumina boat filled with 500 mg pre-prepared WO_3 powder (Sigma-Aldrich, 99.9%) was located at the center of a furnace, and the cleaned sapphire substrates were placed facing down on the boat with WO_3 powder as illustrated in Fig. S1.† A separate boat with sulfur powder (Sigma-Aldrich, 99.5%) was located at the upstream of the furnace, which was heated up to the sulfur evaporation temperature at 120 °C with a heating belt during the growth of monolayer WS_2. The CVD chamber was initially pumped down to a base pressure of ~1 mTorr for 5 minutes and maintained at 15 torr with a 100 sccm flow of argon gas during the synthesis process. The furnace was then heated from room temperature to 200 °C and the temperature was kept constant for 10 minutes to evaporate the water vapor in the quartz tube. The temperature was then further heated up to 950 °C at a ramp rate of 25 °C per min and kept constant for 10 minutes. Finally, the growth chamber was cooled down to room temperature naturally. For the hydrogenated environmentally synthesized WS_2 (HWS_2) sample, the growth process was the same as that described above with commercially available WO_3 powder except that 5% hydrogen gas is introduced into the tube furnace during the growth process.

DFT calculation of the WO_3 crystal structure

DFT calculations were performed on the crystal structure of WO_3 with and without oxygen vacancies. Our calculations were based on density functional theory (DFT) using plane-wave pseudopotentials with the exchange-correlation of Perdew–Burke–Ernzerhof (PBE)[35,36] form as implemented in the Vienna *Ab initio* Simulation Package (VASP).[37] A cutoff energy of 500 eV was employed for the plane wave expansion of the wave functions. The Brillouin zone was sampled with a $9 \times 5 \times 5$ Monkhorst–Pack *k*-point mesh[38] for the structural optimization. The convergence criteria for the total energy and ionic forces were set to 10^{-5} eV and 0.005 eV $Å^{-1}$ respectively. Spin polarization was carefully tested and no spin-polarization effect was observed in our calculations.

Characterization

Photoluminescence (PL) and Raman measurements were obtained with a Witec Alpha300 Confocal Raman system with a laser excitation wavelength of 532 nm and grating density of 600 and 1800 mm^{-1} respectively. X-ray photoelectron spectroscopy (XPS, PHI Quantera II) with a monochromatic Al Kα source (1486.69 eV), operated at a base pressure of 10^{-7} Pa, was employed to obtain the chemical configuration spectra. X-ray diffraction (XRD, Bruker D8) with a Cu Kα source was employed to identify the crystalline phases and structures of the prepared

WO_3 powders. The annular dark field scanning transmission electron microscope (ADF-STEM) image was captured on an aberration-corrected JEOL ARM-200F equipped with a cold field emission gun, operating at 80 kV. The convergence semi-angle of the probe is ~30 mrd. STEM-ADF images were captured for a half angle range from ~85 to 280 mrd. A dwell time of 19 μs per pixel was set for a single-scan image.

Transfer

The as-grown monolayer WS_2 on sapphire was first spin coated with a thin layer of poly(methyl methacrylate) (PMMA) for one minute at a spin speed of 2000 rpm. Then, the edges of the sapphire substrate were removed and the substrate was immersed slowly in a hot solution of 3 mol L^{-1} NaOH (160 °C) to detach the PMMA layer from the sapphire substrate. The resulting sample was then delaminated in deionized water and washed a few times in deionized (DI) water. Finally, the sample was transferred onto a target substrate and carefully blow-dried with nitrogen gas. The PMMA coating was finally removed by using hot acetone vapor at 120 °C for 15 minutes. The samples for STEM study were prepared onto 200 mesh Quantifoil R2/1 micromachined copper grids from SPI Supplies, Structure Probe, Inc. using the same transfer method.

Results and discussion

Generally, the synthesis of 2D TMDCs with the chemical vapor deposition method is based on the direct competition and multiple elementary processes in two reaction pathways between the transition metal suboxide and sulfur. The reaction pathways consist of: (1) transition metal suboxide diffuses and adsorbs on the substrate, and then reacts with S to form monolayer TMDC; (2) transition metal suboxide directly reacts with S in the gas phase to form a TMDC and the resulting WS_2 clusters adsorb, nucleate and form on the substrate.[22,32] Both of the two reaction routes strongly rely on the evaporation and stable delivery of the tungsten source. The metastable state tungsten suboxide can provide a much easier control over the supply of the tungsten source, and thus facilitate the growth process and enhance the growth of WS_2 monolayers. Therefore, the formation of tungsten suboxide plays a critical role in the nucleation and crystallization of TMDC monolayers. In a previous report, in order to promote the growth of monolayer WS_2, hydrogen gas was introduced during the synthesis, which assists the reduction of tungsten trioxide.[16,24,25] Fig. 1a illustrates the synthesis process of monolayer WS_2 in an Ar/H_2 atmosphere in which hydrogen gas acts as a tungsten trioxide reductant to reduce tungsten oxide to form volatile tungsten suboxides ($WO_3 + xH_2 \rightarrow WO_{3-x} + xH_2O$).[16,25,39] The resulting WO_{3-x} are readily volatile, easily evaporate and release the tungsten source.[40–42] The rapid evaporation of the tungsten source will eventually lead to an increase of nucleation sites and hence promote the growth of WS_2.[24,25] Unfortunately, the excessive supply of hydrogen has etching effects on WS_2 ($WS_2 + 2H_2 \rightarrow W + 2H_2S$).[16,25] The excess hydrogen in the growth atmosphere will react with the as-grown WS_2 flakes and remove the sulfur elements, resulting in sulfur vacancies. Precursor pre-treatments such as thermal annealing and plasma treatment create oxygen vacancies in WO_3, resulting in WO_{3-x} (see Fig. 1b). The formation of volatile WO_{3-x} suggests great potential in promoting the growth of monolayer WS_2. Herein, to reveal the effects of oxygen vacancies in WO_3 on the growth of WS_2 monolayers, various tungsten trioxide powders with different oxygen vacancies were prepared, including thermally annealed WO_3 (AWO_3) powder, air plasma treated WO_3 ($PTWO_3$) powder, air plasma treated and annealed WO_3 ($PTAWO_3$) powder, and commercially available WO_3 powder (FWO_3). We first employed AWO_3 powder to obtain the optimized WS_2 growth temperature under the same pressure of 15 torr (see Fig. S1†). As illustrated in Fig. S1,† an optimized growth temperature of 950 °C was determined for WS_2 monolayer synthesis.

We further compared the as-grown WS_2 monolayers produced from the four WO_3 sources with different pre-treatment methods. The growth of monolayer WS_2 strongly depends on the growth conditions, and in order to exclusively probe the effects of WO_3 precursors on the CVD synthesis, regardless of

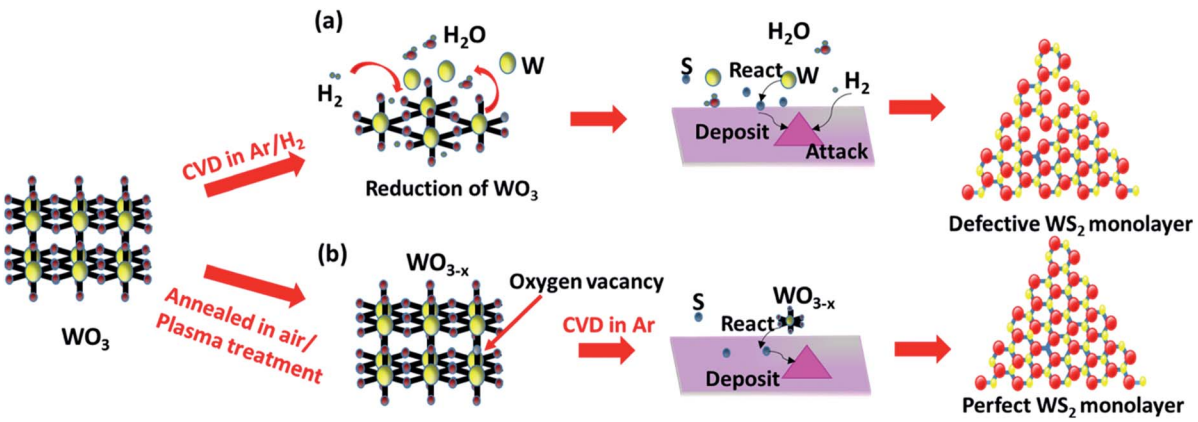

Fig. 1 Reaction mechanism for CVD growth of (a) the commercial precursor in an Ar/H_2 atmosphere; (b) pretreated precursors in an Ar only atmosphere.

the precursor pre-treatment methods used, all the growth processes were carried out under the same growth conditions with a growth temperature of 950 °C and a growth time of 10 minutes. AFM analysis and Raman characterization (see Fig. S2 and S3†) were carried out to confirm the monolayer nature of the WS_2. The AFM line profiles at the edge of all the samples demonstrate that the thicknesses are in the 0.6 nm to 0.9 nm range, which fall in the thickness range of monolayer WS_2. The thickness value differences in such a small range are commonly observed due to the sample's surface conditions. We further compare their Raman peaks, and the samples show two characteristic peaks of monolayer WS_2: a sharp one at 355 cm^{-1} assigned to E_{2g} mode and a broad one at 355 cm^{-1} assigned to A_{1g} mode, matched well with previously reported Raman characterization of monolayer WS_2.[15,16,43] Therefore, all the samples studied in our work are monolayer WS_2, and changing the precursor treatment conditions has no effects on the sample's thickness. According to the statistical analysis over an area of 1000 μm × 750 μm on the growth substrate (see Fig. S4†), the growth size of the monolayer WS_2 is greatly influenced by the type of precursor. An average size of less than 10 μm for WS_2 monolayers was obtained with the FWO_3 precursor, while WS_2 monolayers with a maximum size of ~70 μm and an average size of ~40 μm could be achieved with the AWO_3 precursor. WS_2 monolayers with reduced density and an average lateral size of ~10 μm were obtained when the precursor was changed from FWO_3 to $PTWO_3$. Interestingly, a simple annealing process on the $PTWO_3$ precursor resulted in WS_2 monolayers with an average lateral size of ~20 μm and improved surface coverage on the growth substrate. Besides, as shown in the optical images in Fig. 2a–d, truncated triangular shaped monolayer WS_2 crystals were obtained with FWO_3 and $PTWO_3$ precursors, while WS_2 monolayers in a regular triangular shape could be achieved with AWO_3 and $PTAWO_3$ precursors, revealing the morphology modification caused by the various precursor pre-treatment processes. The photoluminescence (PL) properties of WS_2 monolayers in terms of the peak intensity and position can be dramatically changed due to the presence of various excitonic states such as trions, biexcitons and other charge bounded excitons, which strongly depend on the crystal quality and surface charge states of TMDC monolayers.[26,44–47] As illustrated in Fig. 2e–l, the PL peak intensity mapping (Fig. 2e–h) and position mapping results (Fig. 2i–l) show that WS_2 monolayers synthesized from the AWO_3 precursor exhibit a more uniform PL peak intensity across the surface and have dominant PL peak with higher photon energy (~2.0 eV), which is closer to the band gap of WS_2 (2.1 eV),[48] as compared with the other three synthesized samples.

To evaluate the oxygen vacancies in the precursors, we characterized the precursors with X-ray powder diffraction (XRD) as shown in Fig. 3, S5 and S6.† XRD patterns of all the four precursors consist of the monoclinic phase of WO_3 diffraction peaks (see Fig. 3a), showing that the precursor treatment process did not change the crystal phase. However, the enlarged view of the peak ranging from 22 to 26° shows that all the precursors exhibit a peak position shift to a higher diffraction angle as compared to the standard XRD patterns for the monoclinic phase of WO_3 (Fig. 3b). The XRD diffraction peaks from AWO_3 powder exhibit the most significant peak shift (0.1°) to a higher diffraction angle with peak intensity reduction

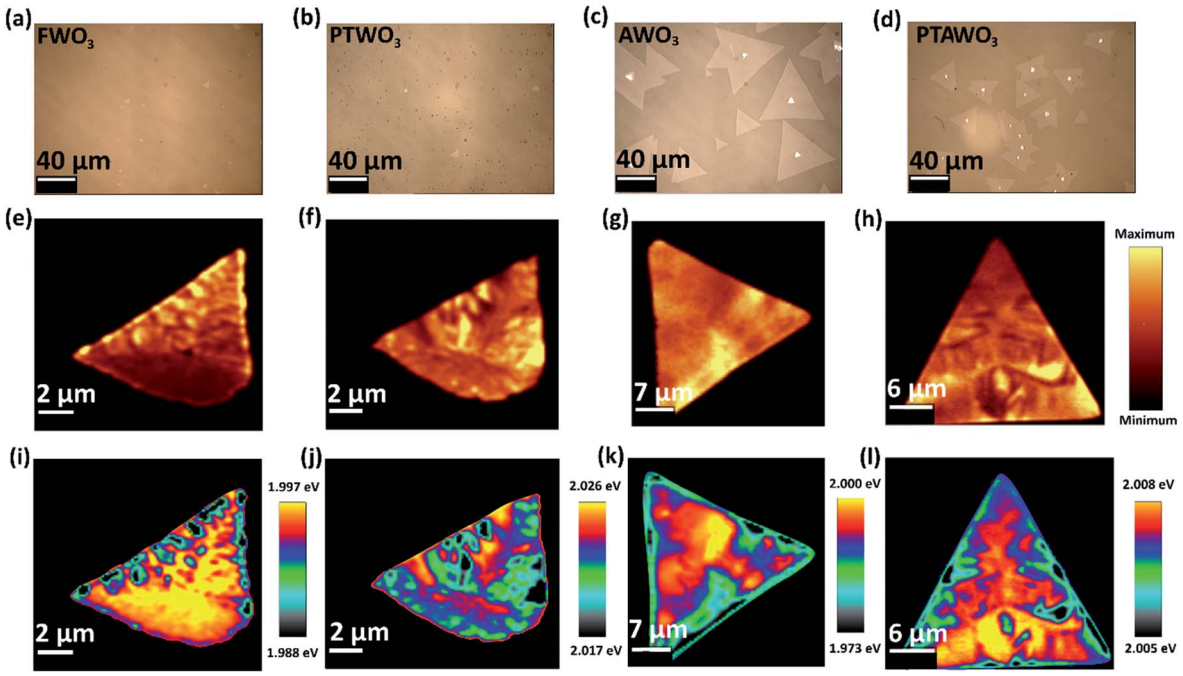

Fig. 2 Optical characterization of the monolayer WS_2 crystals that were obtained from various types of pretreated WO_3 powder. (a–d) Optical images of the monolayer WS_2 crystals that were grown from FWO_3, $PTWO_3$, AWO_3, and $PTAWO_3$ powders, respectively. (e–h) PL intensity mapping images of the monolayer WS_2 crystals that were synthesized from FWO_3, $PTWO_3$, AWO_3 and $PTAWO_3$ powders, respectively. (i–l) PL position mapping images of the monolayer WS_2 crystals that were synthesized from FWO_3, $PTWO_3$, AWO_3 and $PTAWO_3$ powders, respectively.

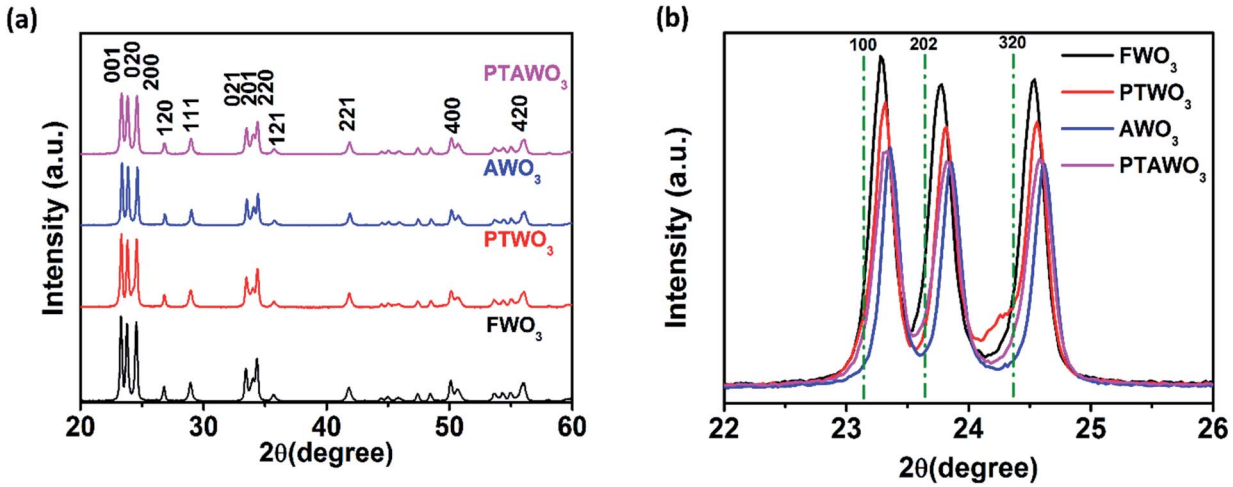

Fig. 3 (a) XRD patterns of FWO_3, $PTWO_3$, AWO_3 and $PTAWO_3$ powders. (b) Enlarged view of XRD patterns at 001, 020 and 200 planes for FWO_3, $PTWO_3$, AWO_3 and $PTAWO_3$ powders.

as compared to FWO_3, followed by $PTAWO_3$ (0.07°) and finally $PTWO_3$ (0.03°). The peak position shifts to a higher diffraction angle are related to the contraction of lattice parameters, which results from the formation of more oxygen vacancies and the degradation of the crystallinity of the WO_3 powder due to the thermal annealing process. As shown in Fig. S7,† WO_3 powders prepared by different methods also show different colors from a greenish color to deep blue and these color changes have been attributed to the different oxygen vacancy contents in WO_3 powders, which is in good consistency with the XRD results.[30,49–51] To eliminate the effects of water content in the precursors on the growth of monolayer WS_2, thermal gravimetric analysis (TGA) (see Fig. S8†) has been done and the results reveal that surface-absorbed water in the WO_3 powders is less than 1%, implying negligible effects on the growth of monolayer WS_2.

To further confirm the oxygen vacancy induced peak position and intensity change in XRD spectra, we further examined the optimized crystal structure of WO_3 with and without oxygen vacancies by theoretical calculations (see Table 1). The lattice structures of WO_3 have been studied using density functional theory (DFT) calculations with plane-wave pseudopotentials.[52] The initial space group of stoichiometric WO_3 is P_{21}/a(#14), belonging to the monoclinic space group. After structural optimization (Fig. 4), the system's space group converts to *Pbcm* (#57). The optimized lattice parameters are $a = 3.904$ Å, $b = 7.778$ Å, and $c = 7.558$ Å. The unit cell volume is 229.54 Å^3, and these four octahedrons in the system are equivalent. For the samples with oxygen vacancies, we remove one oxygen atom from the octahedron from three different directions, namely, *a*-, *b*-, and *c*-axis directions. For oxygen vacancies in the *a*-axis direction, the lattice parameter and volume decrease significantly. For oxygen vacancies in the *b*-axis direction, the bravais lattice shape changes, but the volume is substantially unchanged. For oxygen vacancies in the *c*-axis direction, the lattice constants of *a* and *b* decrease significantly, and the volume also decreases. In practice, oxygen vacancies may exist in any direction, and hence, from the above discussion, we can conclude that the presence of oxygen vacancies will cause the lattice constant of WO_3 to shrink, which explains the peak position shift in XRD spectra for WO_3 with different oxygen vacancy contents.

Moreover, X-ray photoelectron spectroscopy (XPS) analysis exhibits noticeable differences in the binding energy of tungsten and oxygen core levels as illustrated in Fig. 5, S9 and Table S1.† The XPS peak fitting results from all WO_3 powders show that besides the dominating $W4f^{(VI)}$ valence state, a portion of the $W4f^{(V)}$ valence state also exists, confirming the presence of oxygen vacancies in all the WO_3 powders. Yet, the XPS spectral fitting of W4f in AWO_3 and $PTWO_3$ powders suggests a higher contribution from the $W4f^{(V)}$ state as compared with that of FWO_3 powder, indicating the higher oxygen vacancy concentration in both AWO_3 and $PTWO_3$ powders.

Table 1 Calculated optimized structural parameters of WO_3 with and without oxygen vacancies by theoretical calculations

	Lattice parameters (Å)				Angle (Å)		
Crystal structure of WO_3	*a*	*b*	*c*	Volume	*α*	*β*	*γ*
Without Oxygen vacancies	3.904	7.778	7.558	229.54	90.00	90.00	90.00
Oxygen vacancies in the *a*-axis direction	3.796	7.799	7.598	224.95	90.00	90.00	90.02
Oxygen vacancies in the *b*-axis direction	3.808	7.795	7.573	229.48	90.00	90.00	90.03
Oxygen vacancies in the *c*-axis direction	3.824	7.651	7.721	225.85	90.84	90.00	90.00

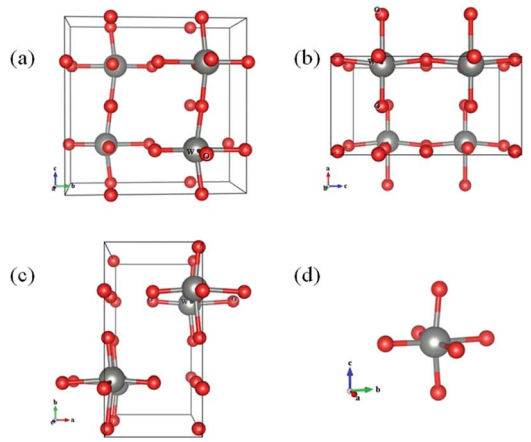

Fig. 4 The view of the optimized structure of WO_3 from the (a) *a*-axis direction, (b) *b*-axis direction, and (c) *c*-axis direction and (d) the octahedron in the WO_3 system. There are 4 W atoms and 12 O atoms in this system.

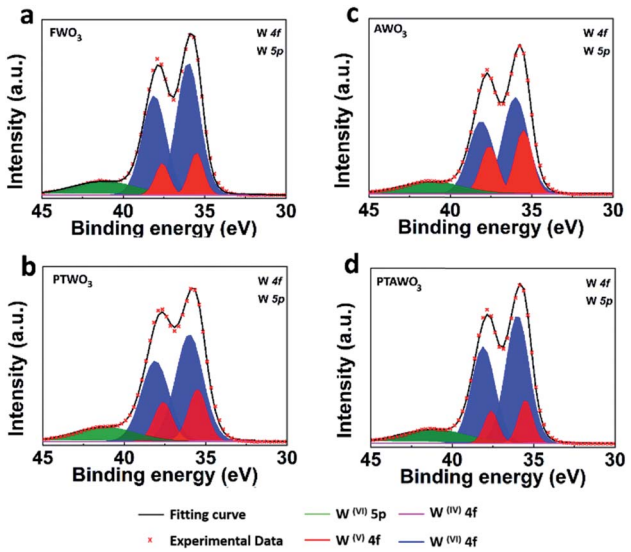

Fig. 5 XPS spectra fitting of W4f and W5p peaks for WO_3 powders. (a–d) XPS spectra of W4f for FWO_3, $PTWO_3$, AWO_3 and $PTAWO_3$ powders, respectively.

Remarkably, compared with the other three control samples, a continuous dark oxide layer was formed after the plasma treatment of WO_3 powder (Fig. S7b†). As reported by Wang *et al.*, Raman spectroscopy is an effective way to characterize the crystallinity of WO_3 powder.[27] As illustrated in Fig. S10,† all the WO_3 powders exhibit the two typical dominating Raman peaks of crystalline WO_3 centered at 808 cm^{-1} and 715 cm^{-1}, except the $PTWO_3$ powder which shows a lower peak intensity and broader stretching mode peak at around 808 cm^{-1}. The significant difference in Raman spectra suggests a strong plasma treatment effect on the surface crystallinity of WO_3.

In fact, XPS analysis shows that the $W4f^{(V)}$ surface state is slightly reduced by thermal annealing for the $PTWO_3$ samples, which could be due to the increased surface oxidation rate towards linear kinetics after plasma treatment.[53] Therefore, the $PTAWO_3$ powder possesses more $W4f^{(VI)}$ surface state compared with $PTWO_3$. It is also noticed that XPS analysis and Raman characterization mainly reflect the surface information of chemical composition; meanwhile XRD presents the crystallinity of bulk sample powders. As shown in Fig. 3b, the XRD diffraction peaks from $PTAWO_3$ powder exhibit a peak shift to a higher diffraction angle and peak intensity reduction, suggesting more oxygen vacancies formed by the annealing process. Combining the XRD, theoretical calculation and XPS analysis, we reach a conclusion that both thermal annealing and plasma treatment lead to the oxygen vacancy formation, while plasma treatment mainly affects the surface chemical states and the thermal annealing process can significantly change the metal oxide crystallinity and result in a smaller lattice spacing. Obviously, combining the precursor characterization and growth results, large-size triangular WS_2 monolayer flakes could be produced with a higher oxygen vacancy concentration in the WO_3 precursor source, while small-size truncated WS_2 monolayers were generally obtained when the number of oxygen vacancies in the WO_3 precursor reduced. The obtained morphology of the as-growth WS_2 is largely related to the reaction conditions, such as the precursor concentration ratio, substrates used, gas flow rate. In pretreated precursors, the highly volatile tungsten suboxide will result in an increase of the amount of tungsten precursors, increase the rate of reaction toward sulfur and hence promote the growth of WS_2. Overall, the thermal annealing process generates more oxygen vacancies in the WO_3 precursor, which effectively promotes the growth of WS_2 monolayers with larger size and better crystallinity. Besides, the PL results also suggest that the monolayer WS_2 samples synthesized from thermal annealing pretreated precursors may have a lower lattice structure defect concentration.

To better reveal the superiority of the monolayer WS_2 obtained from the AWO_3 powder, we further explored the effect of the annealing atmosphere on the structure of the WS_2. As aforementioned above, in previous studies, hydrogen gas (H_2) was introduced to promotes the reduction of WO_3 and hence promote the growth of WS_2 monolayers.[16,19,26,44] However, an excessive hydrogen supply could also induce defects. Therefore, we further study the quality of WS_2 monolayers synthesized with a thermally annealed precursor. The thermally annealed precursor synthesized WS_2 (AWS_2) sample shows a uniform PL intensity feature on the whole surface and still retains its optical properties after being transferred onto a silicon dioxide substrate or more than one-month after the synthesis (see Fig. S11 and S12†). There is no aggregation/restacking effect observed for the AWS_2 monolayers for prolonged periods (after one month). The optical image and optical characterization such as Raman and PL characterization (see Fig. S12†) show the good stability of the as-grown monolayer AWS_2 after being exposed to ambient air for more than one month. The XPS spectra of W4f and S2p peak in AWS_2 as shown in Fig. S13† confirm the presence of WS_2.

Besides, atomic resolution annular dark field scanning transmission electron microscope (ADF-STEM) *Z*-contrast

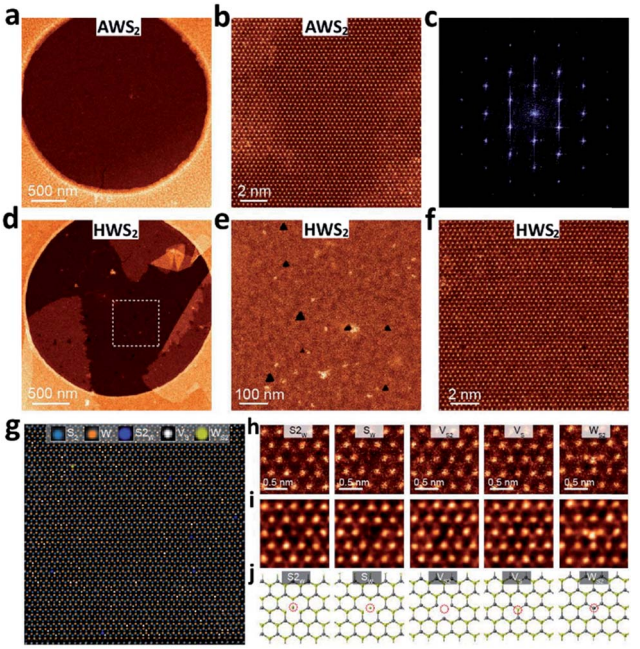

Fig. 6 Atomic structure of monolayer WS_2. (a) STEMADF image of the as-transferred AWS_2 monolayer onto a Quantifoil grid. (b) Atomic resolution ADF/STEM image of the AWS_2 crystal. (c) SAED patterns of the WS_2 crystal. (d) STEMADF image of the as-transferred HWS_2 monolayer onto a Quantifoil grid. (e–f) Atomic resolution ADF/STEM image of the HWS_2 crystal. (g) Defect mapping of the HWS_2 monolayer. (h) Atomic resolution ADF/STEM images of various intrinsic point defects present in monolayer HWS_2, including monosulfur vacancies (V_s), disulfur vacancies (V_{S2}), and antisite defects where a W atom substituting a S_2/S column (W_{S2}, Ws) or a S_2 column substituting a W atom ($S2_w$) is observed. (i) Processed atomic resolution ADF/STEM image of various intrinsic point defects present in monolayer HWS_2. (j) Relaxed structural models of the experimentally observed point defects of HWS_2.

images for the AWS_2 and hydrogenated environmentally synthesized WS_2 (HWS_2) samples were also obtained to study the atomic defect level in both samples (see Fig. 6). The obtained ADF-STEM image and the defect mapping analysis (see Fig. 6b and S14†) show that the AWS_2 sample is almost defect-free, while there are a considerable number of lattice defects, including monosulfur vacancies (V_s), disulfur vacancies (V_{S2}), and antisite defects where a W atom substituting a S_2/S column (W_{S2}, W_S) or a S_2 column substituting a W atom($S2_w$) is observed in the HWS_2 sample (see Fig. 6d–j). These results suggest that the HWS_2 sample contains more lattice defects than the AWS_2 sample. This clearly illustrated that the AWS_2 exhibits better crystallinity and fewer structural defects.

Conclusions

In conclusion, we have comprehensively studied the effects of various stoichiometric WO_3 precursors on the growth of WS_2 monolayers. The morphology of WS_2 monolayers transforms from a truncated triangle to a triangular shape when the oxygen vacancies in the WO_3 precursor increase, resulting in the change of PL properties and crystallinity in the as-growth WS_2 monolayers. The number of oxygen vacancies in WO_3 induces a change in the growth atmosphere and hence significantly affects the lateral growth morphology as well as the optical properties of monolayer WS_2. In our study, the annealed WO_3 precursor with the highest oxygen vacancy concentration generates monolayer WS_2 crystals with improved quality in terms of lateral size, surface coverage, and crystallinity, while $PTWO_3$ and AWO_3 powders with a lower oxygen vacancy concentration suppress the growth of monolayer WS_2. Our results demonstrate the possibility of tailoring the morphology and crystal quality of WS_2 monolayers by the tuning of oxygen vacancy content in the metal oxide precursor. The investigation on various non-stoichiometric WO_3 precursors provides better understanding on the growth mechanism of large-area, high-quality WS_2 monolayers.

Conflicts of interest

There are no conflicts to declare.

Acknowledgements

This work is supported by A*STAR AME IRG (Grant no. A1783c0011). Y. S. acknowledges the support from the Science and Technology Project of Shenzhen (JCYJ20170817101100705), the Thousand Young Talents Program of China, the National Natural Science Foundation of China (Grant no. 51602200) and the (Key) Project of Department of Educational Commission of Guangdong Province (Grant no. 2016KZDXM008). This project was supported by the Shenzhen Peacock Plan (Grant no. KQTD2016053112042971).

References

1 Z. Sun, A. Martinez and F. Wang, *Nat. Photonics*, 2016, **10**, 227–238.
2 G. Grosso, J. Graves, A. T. Hammack, A. A. High, L. V. Butov, M. Hanson and A. C. Gossard, *Nat. Photonics*, 2009, **3**, 577–580.
3 C. Gong, H. Zhang, W. Wang, L. Colombo, R. M. Wallace and K. Cho, *Appl. Phys. Lett.*, 2015, **107**, 139904.
4 H. Tan, Y. Fan, Y. Zhou, Q. Chen, W. Xu and J. H. Warner, *ACS Nano*, 2016, **10**, 7866–7873.
5 A. P. Nayak, Z. Yuan, B. Cao, J. Liu, J. Wu, S. T. Moran, T. Li, D. Akinwande, C. Jin and J. F. Lin, *ACS Nano*, 2015, **9**, 9117–9123.
6 T. Chu, H. Ilatikhameneh, G. Klimeck, R. Rahman and Z. Chen, *Nano Lett.*, 2015, **15**, 8000–8007.
7 W. X. Zhang, Z. S. Huang, W. L. Zhang and Y. R. Li, *Nano Res.*, 2014, **7**, 1731–1737.
8 K. F. Mak, C. Lee, J. Hone, J. Shan and T. F. Heinz, *Phys. Rev. Lett.*, 2010, **105**, 136805.
9 W. Zhao, Z. Ghorannevis, L. Chu, M. Toh, C. Kloc, P. H. Tan and G. Eda, *ACS Nano*, 2013, **7**, 791–797.
10 H. Shi, H. Pan, Y. W. Zhang and B. I. Yakobson, *Phys. Rev. B: Condens. Matter Mater. Phys.*, 2013, **87**, 155304.

11 X. Liu, J. Hu, C. Yue, N. Della Fera, Y. Ling, Z. Mao and J. Wei, *ACS Nano*, 2014, **8**, 10396–10402.
12 M. W. Iqbal, M. Z. Iqbal, M. F. Khan, M. A. Shehzad, Y. Seo, J. H. Park, C. Hwang and J. Eom, *Sci. Rep.*, 2015, **5**, 10699.
13 L. Su, Y. Yu, L. Cao and Y. Zhang, *Nano Res.*, 2015, **8**, 2686–2697.
14 R. K. Ghosh and S. Mahapatra, *IEEE J. Electron Devices Soc.*, 2013, **1**, 175–180.
15 H. R. Gutiérrez, N. Perea-López, A. L. Elías, A. Berkdemir, B. Wang, R. Lv, F. López-Urías, V. H. Crespi, H. Terrones and M. Terrones, *Nano Lett.*, 2013, **13**, 3447–3454.
16 K. M. McCreary, A. T. Hanbicki, G. G. Jernigan, J. C. Culbertson and B. T. Jonker, *Sci. Rep.*, 2016, **6**, 19159.
17 E. J. Sie, J. W. McIver, Y. H. Lee, L. Fu, J. Kong and N. Gedik, *Nat. Mater.*, 2015, **14**, 290–294.
18 H. Zeng, G. B. Liu, J. Dai, Y. Yan, B. Zhu, R. He, L. Xie, S. Xu, X. Chen, W. Yao and X. Cui, *Sci. Rep.*, 2013, **3**, 1608.
19 H. Li, Y. Li, A. Aljarb, Y. Shi and L. J. Li, *Chem. Rev.*, 2018, **118**, 6134–6150.
20 Z. Cai, B. Liu, X. Zou and H. M. Cheng, *Chem. Rev.*, 2018, **118**, 6091–6133.
21 J. Chen, X. Zhao, S. J. R. Tan, H. Xu, B. Wu, B. Liu, D. Fu, W. Fu, D. Geng, Y. Liu, W. Liu, W. Tang, L. Li, W. Zhou, T. C. Sum and K. P. Loh, *J. Am. Chem. Soc.*, 2017, **139**, 1073–1076.
22 Y. Shi, H. Li and L. J. Li, *Chem. Soc. Rev.*, 2015, **44**, 2744–2756.
23 S. L. Wong, H. Liu and D. Chi, *Prog. Cryst. Growth Charact.*, 2016, **62**, 9–28.
24 Y. Sheng, H. Tan, X. Wang and J. H. Warner, *Chem. Mater.*, 2017, **29**, 4904–4911.
25 S. H. Choi, S. Boandoh, Y. H. Lee, J. S. Lee, J. H. Park, S. M. Kim, W. Yang and K. K. Kim, *ACS Appl. Mater. Interfaces*, 2017, **9**, 43021–43029.
26 K. N. Kang, K. Godin and E.-H. Yang, *Sci. Rep.*, 2015, **5**, 13205.
27 X. Zhao, J. Feng, S. Chen, Y. Huang, T. C. Sum and Z. Chen, *Phys. Chem. Chem. Phys.*, 2017, **19**, 1074–1082.
28 Z. Lou and C. Xue, *CrystEngComm*, 2016, **18**, 8406–8410.
29 G. Wang, Y. Yang, Y. Ling, H. Wang, X. Lu, Y. C. Pu, J. Z. Zhang, Y. Tong and Y. Li, *J. Mater. Chem. A*, 2016, **4**, 2849–2855.
30 R. Chatten, A. V. Chadwick, A. Rougier and P. J. D. Lindan, *J. Phys. Chem. B*, 2005, **109**, 3146–3156.
31 W. Wang, A. Janotti and C. G. Van de Walle, *J. Mater. Chem. C*, 2016, **4**, 6641–6648.
32 J. D. Cain, F. Shi, J. Wu and V. P. Dravid, *ACS Nano*, 2016, **10**, 5440–5445.
33 Y. Shi, C. Hamsen, X. Jia, K. K. Kim, A. Reina, M. Hofmann, A. L. Hsu, K. Zhang, H. Li, Z. Y. Juang, M. S. Dresselhaus, L. J. Li and J. Kong, *Nano Lett.*, 2010, **10**, 4134–4139.
34 Y. Shi, H. Li, J. I. Wong, X. Zhang, Y. Wang, H. Song and H. Y. Yang, *Sci. Rep.*, 2015, **5**, 10378.
35 J. P. Perdew, K. Burke and M. Ernzerhof, *Phys. Rev. B: Condens. Matter Mater. Phys.*, 1996, **77**, 3865–3868.
36 G. Kresse and D. Joubert, *Phys. Rev. B: Condens. Matter Mater. Phys.*, 1999, **59**, 1758–1775.
37 G. Kresse and J. Furthmüller, *Phys. Rev. B: Condens. Matter Mater. Phys.*, 1996, **54**, 11169–11186.
38 H. J. Monkhorst and J. D. Pack, *Phys. Rev. B: Solid State*, 1976, **13**, 5188–5192.
39 M. G. Charlton, *Nature*, 1954, **174**, 703.
40 N. Birks, G. H. Meier and F. S. Pettit, *Introduction to the High Temperature Oxidation of Metals*, Cambridge University Press, Cambridge, 2 edn, 2006.
41 V. K. Sarin, *J. Mater. Sci.*, 1975, **10**, 593–598.
42 P. K. Sahoo, S. Memaran, Y. Xin, L. Balicas and H. R. Gutiérrez, *Nature*, 2018, **553**, 63.
43 M. S. Kim, S. J. Yun, Y. Lee, C. Seo, G. H. Han, K. K. Kim, Y. H. Lee and J. Kim, *ACS Nano*, 2016, **10**, 2399–2405.
44 S. Paradisanos, N. T. Germanis, C. Pelekanos, E. Fotakis, E. Kymakis, G. Kioseoglou and E. Stratakis, *Appl. Phys. Lett.*, 2017, **110**, 193102.
45 Y. C. Lin, S. Li, H. P. Komsa, L. J. Chang, A. V. Krasheninnikov, G. Eda and K. Suenaga, *Adv. Funct. Mater.*, 2018, **28**, 1704210.
46 J. H. Yun, J. Youngjo, Y. S. Joon, Z. Jiong, B. Jaeyoon, K. D. Hoon, L. H. Seok and L. Y. Hee, *Adv. Mater.*, 2017, **29**, 1605043.
47 G. Plechinger, P. Nagler, J. Kraus, N. Paradiso, C. Strunk, C. Schüller and T. Korn, *Phys. Status Solidi RRL*, 2015, **9**, 457–461.
48 X. H. Wang, J. Q. Ning, Z. C. Su, C. C. Zheng, B. R. Zhu, L. Xie, H. S. Wu and S. J. Xu, *RSC Adv.*, 2016, **6**, 27677–27681.
49 C. G. Granqvist, *Handbook of Inorganic Electrochromic Materials*, Elsevier, 1995.
50 G. Wang, Y. Ling, H. Wang, X. Yang, C. Wang, J. Z. Zhang and Y. Li, *Energy Environ. Sci.*, 2012, **5**, 6180–6187.
51 Y. Djaoued, S. Balaji and R. Brüning, *J. Nanomater.*, 2012, **2012**, 9.
52 J. Ihm, A. Zunger and M. L. Cohen, *J. Phys. C: Solid State Phys.*, 1979, **12**, 4409.
53 S. C. Cifuentes, M. A. Monge and P. Pérez, *Corros. Sci.*, 2012, **57**, 114–121.

